CHEMISTRY OF MATERIALS

pubs.acs.org/cm

Article

Scalable High-Performance $Li_2Zr_{0.2}Ta_{0.8}OCl_{4.8}$ Solid Electrolytes: Structure, Dynamics, and Stability

Thilina N.D.D. Gamaralalage,[‖] Bright O. Ogbolu,[‖] M.D. Mahinur Islam, Tehreem Toheed, Joey Peterson, Tej P. Poudel, and Yan-Yan Hu*

Cite This: *Chem. Mater.* 2026, 38, 7095−7103

Read Online

ACCESS | Metrics & More | Article Recommendations | Supporting Information

ABSTRACT: High-performance solid electrolytes (SEs) are vital for advancing all-solid-state batteries (ASSBs) by improving safety, energy density, and longevity. While halide-based SEs offer excellent oxidative stability, further improvements in interfacial compatibility, ion transport, and efficient synthesis are still needed. Here, we introduce $Li_2Zr_{0.2}Ta_{0.8}OCl_{4.8}$ (LZTOC), an amorphous oxychloride SE synthesized via a single-step, 2-hour mechanochemical process that eliminates high-temperature processing and hazardous byproducts, such as HCl gas. Structural characterization by XRD, Raman, and high-resolution NMR confirms an amorphous oxychloride framework with locally preserved Ta/Zr coordination motifs bridged by oxygen, thereby supporting a percolating ion-transport network. NMR relaxation measurements indicate enhanced Li^+ mobility relative to Li_2ZrCl_6 and Li_2ZrOCl_4. Electrochemical measurements reveal a high ionic conductivity of 6.17 mS cm^{-1} and low activation energy ~0.30 eV for LZTOC. Battery cycling tests with uncoated NMC811 as the cathode active material and LZTOC as the catholyte and separator deliver ~88.9% capacity retention and an excellent Coulombic efficiency over 99.8% at extended cycles. These results position LZTOC as a scalable, high-performance oxychloride SE, where partial Zr-substitution improves cost-effectiveness relative to purely Ta-based analogues, for next-generation ASSBs.

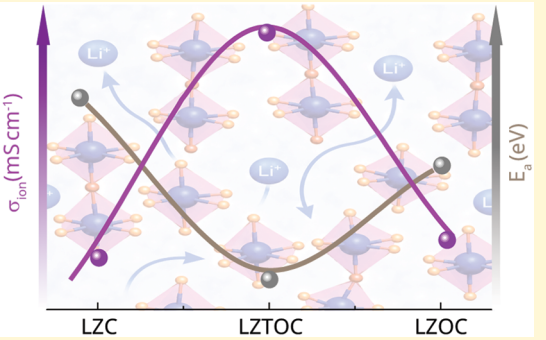

INTRODUCTION

The development of high-performance solid electrolytes (SEs) is essential for advancing all-solid-state batteries (ASSBs), which offer improved safety, energy density, and cycle life compared to traditional liquid-electrolyte-based systems.[1,2] Among different SEs, halide-based SEs have gained significant interest due to their ionic conductivity, low grain boundary resistance, and compatibility with high-voltage cathodes.[3] However, many halide SEs still struggle with reduction instability against the Li anode, moisture sensitivity, and processing difficulties, which hinder their practical scalability.[4] Representative halide-based SEs, such as Li_3YCl_6, Li_3InCl_6, and Li_2ZrCl_6, have shown the potential of halide conduction networks for fast lithium-ion transport.[5−7] Yet their synthesis often requires high-temperature routes or extended milling times (20 h to days), which makes large-scale production difficult.[1,8] Additionally, the rigid anion sublattice in purely halide-based materials can limit structural flexibility, impacting interfacial and long-term performance.[9]

A further limitation is cost: many high-performing halide SEs rely on scarce and expensive cations (Y, Er, Ho, Sc, In), reducing their viability for large-scale deployment.[10] A notable exception is the recently reported Li_2ZrCl_6 (LZC), which uses abundant Zr but exhibits <1 mS cm^{-1} conductivity at 25 °C, insufficient to form an effective percolating ion-conduction network when used as a separator or catholyte.[8] Aliovalent substitution has been explored to improve LZC, including $Li_{2.25}Zr_{0.75}Fe_{0.25}Cl_6$ (0.98 mS/cm),[10] $Li_{5/3}Cr_{1/3}Zr_{1/3}Cl_4$ (0.31 mS/cm),[11] $Li_{2.1}Zr_{0.9}La_{0.1}Cl_6$ (0.082 mS/cm),[12] $Li_{2.1}Zr_{0.95}Ca_{0.05}Cl_6$ (0.58 mS/cm),[13] and $Li_{1.25}Zr_{0.375}Mg_{0.625}Cl_4$ (0.014 mS/cm).[14] But the conductivity gains have remained modest, particularly within the common +2/+3 cation dopant space. In parallel, mixed-anion strategies have emerged as an effective route to accelerate ion transport in halide frameworks.[15] Oxygen substitution in chloride-type systems (L-M-Cl, M = Ta/Nb) yields oxyhalides with conductivities exceeding 10 mS cm^{-1},[1] and applying oxygen incorporation to Zr-halide frameworks has increased LZC-derived conductivities into the >1 mS cm^{-1} range.[8,16] These results motivate a combined design approach that leverages the scalability and cost advantages of Zr while using targeted chemical tuning to unlock higher conductivity.[17]

Received: January 17, 2026
Revised: June 15, 2026
Accepted: June 18, 2026
Published: July 6, 2026

Here, we pursue a simultaneous cation−anion substitution strategy, guided by chemical principles that connect bonding characteristics, polarizability, and ion migration barriers. A key approach is the use of high ionic-potential cations, which can withdraw electron density from neighboring anions. This weakens Li-anion interactions, resulting in a flatter energy landscape and lower activation barriers for Li^+ transport. These trends align with periodic behavior in polarizability. Ionic polarizability generally decreases across a period and increases down a group, resulting in the diagonal relationship observed in the periodic table. Diagonally related elements often share similar chemical behavior, making them useful for targeted substitutions in solid electrolytes.[18] In this context, Ta, which has a higher chemical potential (ϕ_m = 78.13 nm^{-1}) than Zr (ϕ_m = 55.56 nm^{-1}), is a promising and structurally compatible substitute for Zr in solid-state electrolytes;[19] it may serve as an inductive lever to enhance Li^+ motion.

We therefore focus on oxychlorides, where oxygen modifies the anion framework and drive disorder.[20,21] While Li−Zr−O−Cl compounds (LZOC) benefit from improved chemical robustness, their conductivity and transport mechanism remain less favorable and incompletely understood, and Li_2TaOCl_4 (LTOC), although more conductive, is commonly synthesized using LiOH routes that can release hazardous HCl gas and raise scalability concerns.[1,2] By integrating Ta^{5+} into LZOC, we introduce $Li_2Zr_{0.2}Ta_{0.8}OCl_{4.8}$ (LZTOC), synthesized via a rapid, single-step, 2-hour mechanochemical process that avoids high-temperature sintering and LiOH, with no HCl emissions. This strategy is further motivated by application demands: conductivity losses at low temperatures severely limit ASSB operation in cold climates,[22] yet LZTOC maintains 1.16 mS cm^{-1} at −10 °C, indicating improved low-temperature kinetics. The amorphous nature of LZTOC also provides practical processing advantages, including isotropic transport, minimal grain-boundary resistance, and mechanical compliance that enables cold pressing to produce dense, low-tortuosity catholytes.[23,24] Importantly, while solid electrolytes typically comprise 40−60 wt % of the catholyte and act as electrochemically inactive mass, recent studies show that high-valent cations such as Ta^{5+} and Nb^{5+} can undergo reversible redox activities, enabling the electrolyte to contribute directly to capacity. The Ta^{5+} in LZTOC therefore enhances lithium mobility, reinforces structural stability, and helps address the "dead weight" limitation in conventional catholytes, offering a dual-functional design that improves both energy density and low-temperature operability in ASSBs.[24]

This work establishes LZTOC as a high-performance amorphous oxychloride solid electrolyte enabled by a rapid mechanochemical synthesis. XRD, Raman, and high-resolution NMR show a clear evolution from crystalline LZC to amorphous LZOC and finally LZTOC, with Ta incorporation promoting an oxygen-bridged network of Ta/Zr-centered motifs that supports percolative Li^+ transport. LZTOC achieves 6.17 mS cm^{-1} ionic conductivity with a low ∼0.30 eV activation barrier, consistent with faster Li^+ dynamics observed from ^{7}Li NMR T_1. In solid-state cells, LZTOC serves as both separator and catholyte, enabling stable cycling with uncoated NMC811, 99.8% Coulombic efficiency, and 88.9% capacity retention, highlighting cation-tuned oxychloride glasses as a scalable route for next-generation ASSBs.

MATERIALS AND METHODS

Synthesis

A stoichiometric mixture of the starting materials, lithium oxide (Li_2O, 99.5%, Alfa Aesar), anhydrous zirconium tetrachloride ($ZrCl_4$, 99.9%, Alfa Aesar), and tantalum pentachloride ($TaCl_5$, 99.99%, Sigma-Aldrich), was manually ground to ensure homogeneity. The resulting powder was then transferred into a 20 mL zirconia milling jar containing three zirconia balls (10 mm in diameter) and vacuum-sealed within the glovebox. Mechanochemical synthesis was carried out using a high-energy ball miller (8000 M Mixer-Mill) for 2 h. After milling, the homogenized powder was returned to the argon-filled glovebox (MBraun) and stored under inert conditions for subsequent characterization.

Powder X-ray Diffraction (PXRD)—Bragg diffraction patterns for phase and structural determination were collected on a Rigaku SmartLab diffractometer operated in Bragg−Brentano geometry using Cu Kα radiation (λ = 0.154 nm). Data was recorded over a range of 2θ angles from 10° to 70° with step increments of 0.03° with a 1.5 s counting time per step. Powder samples were mounted on zero-background sample holders and enclosed with Kapton film under an inert argon atmosphere to avoid atmospheric contamination prior to analysis.

Solid-State NMR

^{6}Li and ^{7}Li magic angle spinning (MAS) NMR measurements were carried out on a Bruker Avance III spectrometer fitted with an Ultrashield 500 MHz (11.74 T) wide-bore (89 mm) magnet. ^{6}Li and ^{7}Li nuclei were observed at 73.6 and 194.4 MHz, respectively. Powdered samples were loaded into 2.5 mm ZrO_2 rotors under an inert argon atmosphere and spun at 24 kHz MAS. Single-pulse experiments employed a 3.3 μs $\pi/2$ pulse and recycle delays of 500 s for ^{6}Li and 50 s for ^{7}Li. To investigate ion dynamics, variable-temperature ^{7}Li NMR T_1 measurements were conducted using a 300 MHz (7.05 T) spectrometer at a Larmor frequency of 116 MHz. All chemical shifts were referenced to solid LiCl at −1.1 ppm.

NMR Calculations

The Li chemical shifts in LZC were calculated using the GIPAW method at the GGA level of theory, as implemented in the Vienna Ab Initio Simulation Package (VASP) version 5.4.4. A total of 15 structures of LZC were generated using the supercell program and used for chemical shift calculations. The structures were initially relaxed using the PBE exchange−correlation functional and utilized a 600 eV cutoff energy for the plane-wave basis, a 2 × 2 × 2 k-point mesh generated according to the Monkhorst−Pack scheme, and an electronic convergence threshold of 10^{-6} eV. Following the relaxation, chemical shifts were calculated using a larger plane-wave basis with an increased cutoff energy of 800 eV and an increased electronic convergence threshold of 10^{-8} eV in a single-point calculation. The k-point mesh was kept the same for the chemical-shift calculations. All ^{7}Li chemical shifts were referenced to LiCl (Crystallography Open Database no. 908665).

Scanning Electron Microscopy (SEM) and Energy Dispersive X-ray Spectroscopy (EDS)

Morphological and elemental distributions were assessed by using a JEOL JSM-7000F field-emission SEM instrument operated at an accelerating voltage of 15 kV. Samples were sputter-coated with iridium and mounted on aluminum stubs employing carbon adhesive tape prior to examination for purposes of yielding adequate conductivity and removing charging artifacts. EDS was concurrently performed with SEM imaging using an Oxford Instruments X-Max detector and Aztec analytical software for quantitative elemental mapping and compositional analysis. A 10 mm working distance was employed to optimize spatial resolution and X-ray detection efficiency. All experiments were carried out at room temperature under high-vacuum conditions.

https://doi.org/10.1021/acs.chemmater.6c00149
Chem. Mater. 2026, 38, 7095−7103

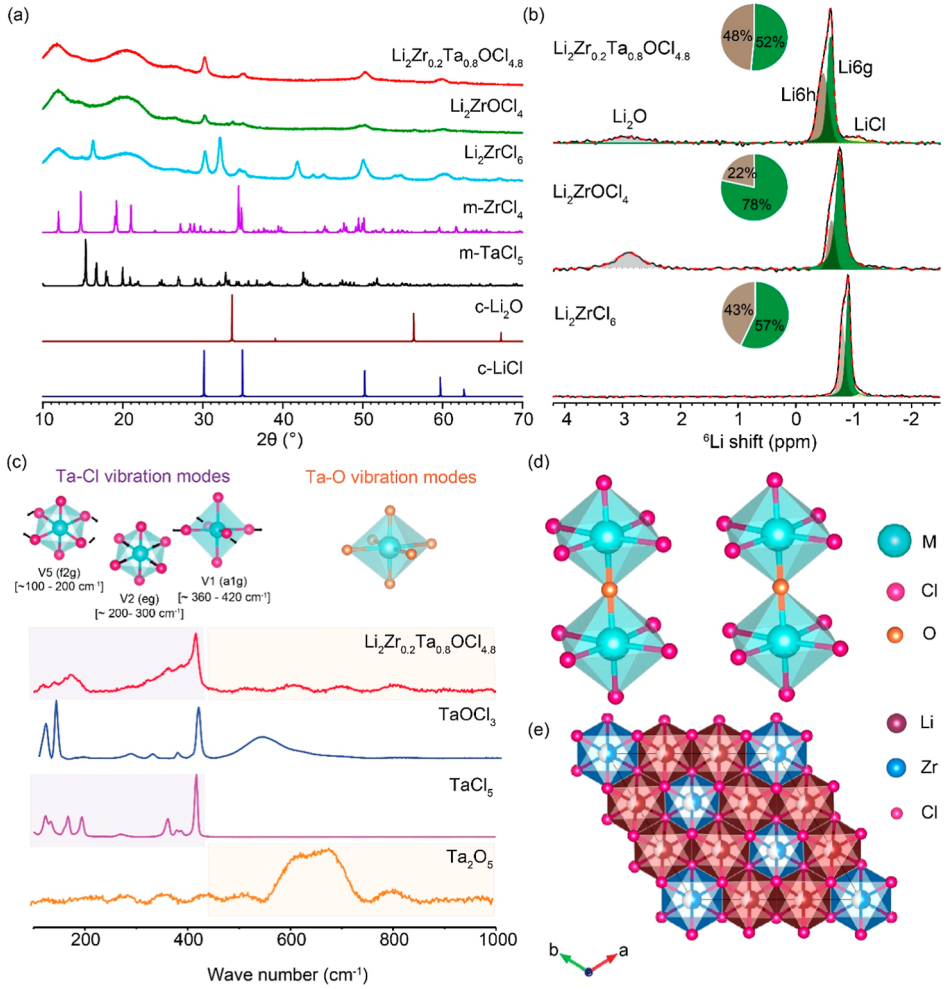

Figure 1. Structure of $Li_2Zr_{0.2}Ta_{0.8}OCl_{4.8}$. The X-ray diffraction patterns of $Li_2Zr_{0.2}Ta_{0.8}OCl_{4.8}$, Li_2ZrOCl_4, and Li_2ZrCl_6, in comparison with the diffraction patterns of LiCl, Li_2O, $TaCl_5$, and $ZrCl_4$. (b) ^{6}Li MAS NMR spectra of Li_2ZrCl_6, Li_2ZrOCl_4, and $Li_2Zr_{0.2}Ta_{0.8}$ $OCl_{4.8}$. (c) Raman spectra of Ta_2O_5, $TaCl_5$, $TaOCl_3$, and $Li_2Zr_{0.2}Ta_{0.8}OCl_{4.8}$ and the corresponding peak assignments. (d) Representative motifs of the anion network in LZTOC based on Raman, NMR, and XRD data. Ta/Zr are six-coordinated with Cl/O in an octahedral environment in LZTOC. (e) Refined structure of Li_2ZrCl_6.

Raman Spectroscopy

Raman measurements were performed on a Horiba JY LabRam HR Evolution spectrometer using a 532 nm excitation source and a 600 grooves mm^{-1} dispersive grating. Spectra were recorded in the range of 100−1000 cm^{-1} at 20 mW laser power and 4 s acquisition time per measurement. Acquisition of data and spectral processing were achieved through LabSpec6 software. Samples were packed in an argon-filled glovebox, and all measurements were made at room temperature under inert conditions.

Electrochemical Impedance Spectroscopy (EIS)

LZTOC samples were hand-ground and pressed in a 10 mm diameter mold to make a ∼0.8 mm thick pellet for impedance measurements. The pellet was assembled in a split cell with stainless steel as the blocking electrode. Potentiostatic EIS was carried out using a Gamry electrochemical analyzer, and conductivities were calculated from the resulting Nyquist plots. Variable-temperature EIS characterization was performed from −20 to 60 °C to calculate the activation energy via Arrhenius plots. The direct current polarization technique with ion-blocking electrodes was used to determine the effective electronic conductivity. Equilibrium currents were monitored at several voltages (100, 200, 300, and 400 mV).

Linear Sweep Voltammetry

A 10 mm diameter pellet was fabricated by loading approximately 80 mg of Li_6PS_5Cl powder into a polyether ether ketone (PEEK) cylinder and compressing it at 250 MPa for 10 s. Subsequently, about 30 mg of LZTOC was uniformly applied to one surface of the SE pellet, followed by another compression step at 250 MPa for 30 s. To prepare the LZTOC−carbon nanofiber composite, LZTOC and carbon nanofiber (Sigma-Aldrich) were combined in a 9:1 weight ratio, then manually mixed and ground in an agate mortar for 15 min. About 8 mg of this composite mixture was evenly applied to the LZTOC surface of the pellet to serve as the working electrode, followed by compression at 300 MPa for 1 min. The opposite surface was fitted with 1.0 mg of Li foil (Sigma-Aldrich) applied by hand pressing. The complete cell assembly was then housed in a stainless-steel casing and maintained under a continuous pressure of 30 MPa. Linear Sweep Voltammetry (LSV) measurements were performed using a BioLogic SP-300 instrument at a scan rate of 0.1 mV/s.

Assembly of ASSB

Half-cells were assembled using custom-designed 10 mm split cell configurations equipped with stainless-steel plungers serving as current collectors. The solid electrolyte pellet was formed by loading approximately 80 mg of Li_6PS_5Cl powder into a PEEK cylinder (10 mm diameter) and compressing it at 250 MPa for 10 s. Subsequently, about 30 mg of LZTOC was uniformly applied to one surface of the SE pellet, followed by another compression step at 250 MPa for 30 s. The composite cathode material was prepared by combining $LiNi0.8Co_{0.10}Mn_{0.10}O_2$ (NMC811) (MSE Supplies), LZTOC, Super P carbon, and PVDF in the ratio of (47.5:47.5:4.7:0.3), then manually

https://doi.org/10.1021/acs.chemmater.6c00149
Chem. Mater. 2026, 38, 7095−7103

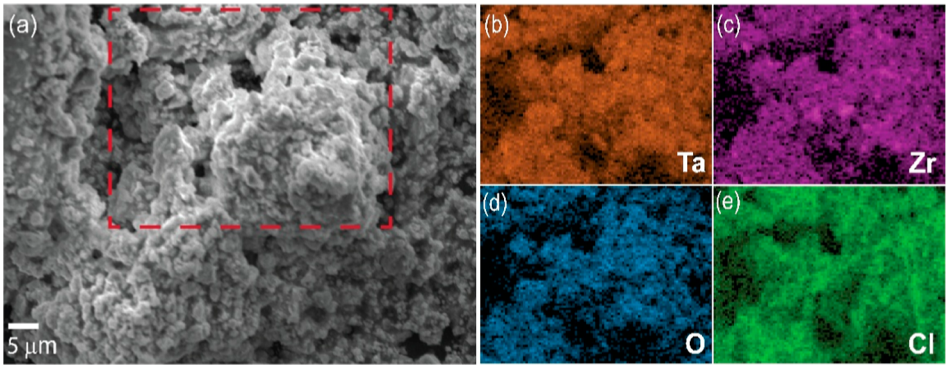

Figure 2. Scanning electron microscopy (SEM) and energy dispersive spectroscopy (EDS) mapping of as-milled $Li_2Zr_{0.2}Ta_{0.8}OCl_{4.8}$, showing uniform elemental distribution.

grinding the mixture in an agate mortar for approximately 20 min. Around 10 mg of this composite material (corresponding to ∼1.41 mAh cm^{-2} capacity) was evenly spread on the LZTOC side and was compressed at 300 MPa. On the Li_6PS_5Cl side, an In foil (27 mg) was placed, followed by Li (1 mg). Cells were cycled at a stack pressure of approximately 30 MPa at lab temperature (22 °C) between 2.1−4.2 V vs. Li−In.

RESULTS AND DISCUSSION

Average and Local Structure Analysis

The powder XRD patterns of LZOC and LZTOC exhibit only weak diffraction peaks from the byproduct LiCl (Figure 1a), indicating a low crystallinity of the main phase. The base material LZC, prepared under similar conditions with 2 h of high-energy ball milling, shows multiple diffraction peaks and crystallizes in the trigonal crystal system (space group p-3m1)[10,25] (Figures S1 and 1e). This transition from a crystalline (LZC) to an amorphous compound (LZOC and LZTOC) upon O^{2-} introduction could be attributed to the disordered anion lattice in LZOC and LZTOC, which has been shown in similar systems to reduce the diffraction intensity of the anionic planes.[26]

Figure 1b shows the ^{6}Li MAS NMR spectra of LZC, LZOC, and LZTOC (See Tables S1−S4 for a summary of the NMR parameters from experimental and calculation data). In LZC, there are two inequivalent Li^+ sites which occupy 6g (Li_{6g}) and 6h (Li_{6h}) Wyckoff positions (Table S5). These two Li^+ sites manifest in ^{6}Li MAS NMR as two resonances with isotropic peaks at −0.9 ppm and −0.8 ppm, respectively. DFT-calculated Li isotropic chemical shifts for Li_{6g} and Li_{6h} sites in LZC (Table S4) show consistent relative positioning with the Li_{6g} site being more upfield than Li_{6h}. The two resonances remain for LZOC but appear downfield-shifted and significantly broadened. The shift in the resonance positions indicates weakened Li^+−Cl^- local interactions, and the peak broadening suggests disordered local environments induced by O incorporation. The broad, low-intensity resonance at 2.8 ppm is attributed to residual Li_2O. A further downfield shift is observed for LZTOC, which correlates with a reduced amount of residual Li_2O, as reflected by the decreased intensity of the corresponding resonance at 2.8 ppm. This further echoes the prior observation of weakened Li^+−Cl^- local interactions with increased O-incorporation, and Ta^{5+} facilitates O-incorporation into the structure. Additionally, LZTOC exhibits a slightly narrower line width (19 Hz) than LZOC (22 Hz). Line width narrowing can often indicate faster Li^+ mobility,[27] this modest reduction should be interpreted qualitatively as reflecting reduced chemical-shift dispersion and partial motional averaging in a disordered Li environment. LiCl is detected in all three samples as a minor component, indicated by the ^{6}Li MAS NMR peak at −1.1 ppm, consistent with the X-ray data (Figure 1a).

A general understanding of the metal coordination environment in LZTOC can be inferred by comparing its Raman spectrum (Figure 1c) with those of well-characterized reference compounds such as $TaCl_5$, $TaOCl_3$, and Ta_2O_5. This comparative analysis provides valuable insights into the chemical composition and bonding characteristics of LZTOC. $TaCl_5$ and $TaOCl_3$ exhibit multiple sharp peaks in the lower wavenumber range (100−400 cm^{-1}), associated with M−Cl vibrational modes.[26] The set of peaks centered between 100−200 cm^{-1} is assigned to the $V_5(f_{2g})$ bending modes. Peaks centered around 300 cm^{-1} are assigned to $V_2(e_g)$ stretching modes. Peaks around 360−400 cm^{-1} are attributed to the $V_1(a_{1g})$ stretching mode, as illustrated in Figure 1c.[28] These peaks are either absent or significantly broadened in LZTOC, suggesting symmetry breaking induced by defects or disorder.[29]

Ta_2O_5 exhibits broad vibrational peaks in the 400−1000 cm^{-1} range, associated with Ta−O stretching vibrations. The higher-energy bands observed within ∼400−800 cm^{-1} are most likely attributed to coupled vibrational modes dominated by different Ta−O stretches, whereas the bands above 800 cm^{-1} correspond to stretching vibrations of Ta−O−Ta linkages.[30,31] Peaks around 800 cm^{-1} indicate that oxygen atoms primarily function as bridging ligands, connecting Ta-centered trigonal bipyramidal units.[21] In LZTOC, broad, low-intensity features are observed in the ∼500−900 cm^{-1} regions that are consistent with Ta−O−Ta (M-*O*-M) stretching modes reported for Ta−O-containing motifs[32] and are also present in the $TaOCl_3/Ta_2O_5$ reference spectra; however, their proximity to the baseline means they cannot be unambiguously distinguished from background in the present data. Therefore, these features are treated as suggestive rather than conclusive evidence for oxygen-bridged Ta-centered connectivity. But, given that $TaOCl_3$ is built from oxychloride polyhedra that can connect through oxygen-containing linkages, LZTOC could plausibly contain Ta−O−Ta chain-like motifs. The significantly reduced intensity of the peak around 650 cm^{-1} attributed to bridging oxygen may be due to structural disorder in LZTOC.[33] Bridging O^{2-} ions play a vital role in determining ionic conductivity. Unlike nonbridging O^{2-}, which strongly interacts with mobile Li^+ ions and hinders their movement, bridging oxygen exhibits minimal interaction,

https://doi.org/10.1021/acs.chemmater.6c00149
Chem. Mater. 2026, 38, 7095−7103

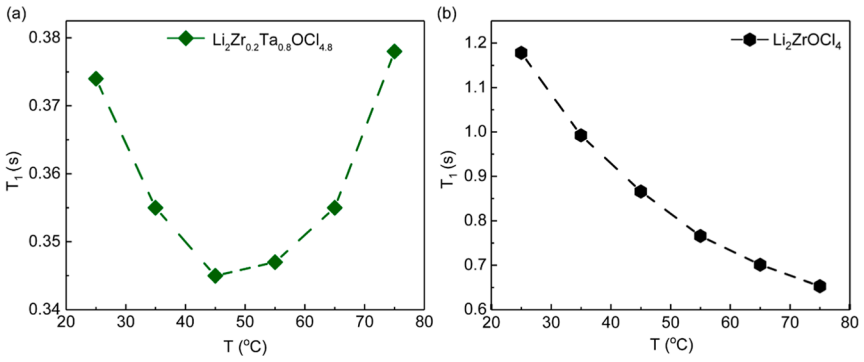

Figure 3. ^{7}Li NMR T_1 relaxation times as a function of temperature for (a) $Li_2Zr_{0.2}Ta_{0.8}$ $OCl_{4.8}$ and (b) Li_2ZrOCl_4.

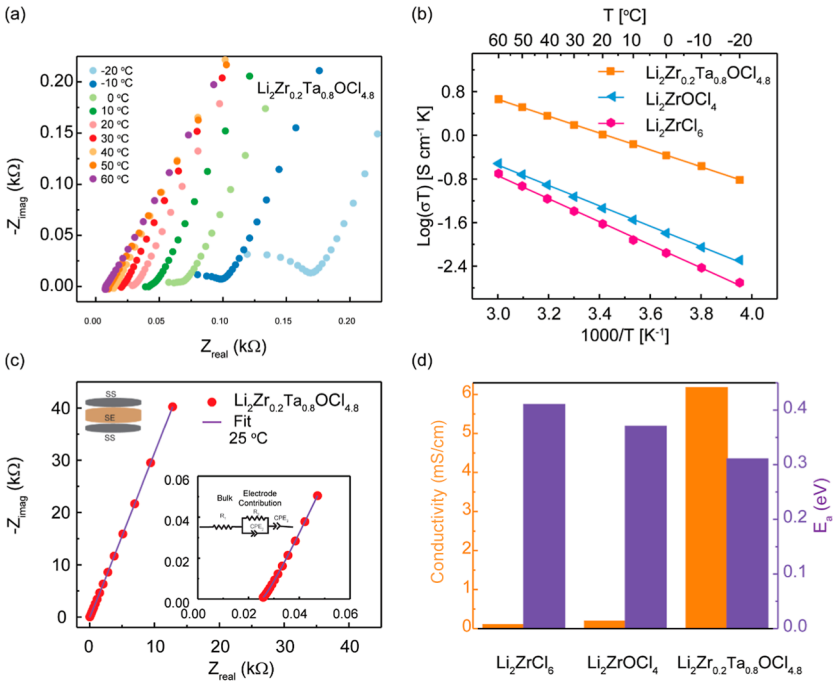

Figure 4. Electrochemical properties of $Li_2Zr_{0.2}Ta_{0.8}$ $OCl_{4.8}$. (a) Nyquist plots of the as-milled $Li_2Zr_{0.2}Ta_{0.8}$ $OCl_{4.8}$measured in the temperature range from −20 to 60 °C. (b) Arrhenius plots of $Li_2Zr_{0.2}Ta_{0.8}OCl_{4.8}$, Li_2ZrOCl_4, and Li_2ZrCl_6 from the temperature-dependent EIS measurements in the temperature range from −20 to 60 °C. (c) Representative Nyquist plot and corresponding equivalent circuit fit of $Li_2Zr_{0.2}Ta_{0.8}$ $OCl_{4.8}$ measured at 25 °C to obtain ionic conductivity. (d) Comparison of the ionic conductivities at 25 °C and activation energies of $Li_2Zr_{0.2}Ta_{0.8}$ $OCl_{4.8}$, Li_2ZrOCl_4, and Li_2ZrCl_6.

thereby facilitating smoother ion transport.[34] Given the chemical similarities and the spectral features observed in reference compounds, it is reasonable to infer that the local environment around the metal cation in LZTOC also adopts a similar octahedral coordination. Therefore, the structural motifs in LZTOC likely consist of Ta-centered octahedra interconnected through oxygen bridges, forming an amorphous yet locally ordered network, as illustrated in Figure 1d.

Sample Morphology

The SEM image in Figure 2 reveals an agglomerated morphology with irregularly shaped particles ranging from submicrometers to several micrometers in size, likely resulting from mechanochemical milling. Elemental mapping using EDS shows a uniform distribution of Ta, Zr, O, and Cl, indicating no phase segregation. Similarly, a homogeneous distribution of elements is observed in the LZC and LZOC samples (Figures S2 and S3), further confirming the effectiveness of the synthesis method across different compositions.

Ion Dynamics from NMR Relaxation Time Measurements

The ^{7}Li NMR spin−lattice relaxation time (T_1) plots for LZTOC and LZOC (Figure 3) exhibit distinct temperature-dependent behaviors, providing insight into lithium-ion dynamics in these amorphous materials. LZTOC exhibits a U-shaped T_1 trend, with a minimum at ∼45 °C, indicating that the lithium-ion motional rate at around 45 °C is near the ^{7}Li Larmor frequency ω_0 of 116.6 MHz. At both lower and higher temperatures, T_1 increases; this behavior aligns with the intermediate motional regime described by the Bloembergen−Purcell-Pound (BPP) theory, *i.e.*, $\omega_0\tau_c = 1$, where τ_c is the time constant for Li^+ motion.[35] Whereas LZOC shows a monotonic decrease in T_1 with temperature, suggesting a slower overall ionic motion, compared with LZTOC. The comparison indicates that the Ta^{5+} substitution in LZTOC enhances lithium-ion mobility, possibly by altering local Li^+−Cl^- interactions and facilitating more efficient Li^+-ion transport.

https://doi.org/10.1021/acs.chemmater.6c00149
Chem. Mater. 2026, 38, 7095−7103

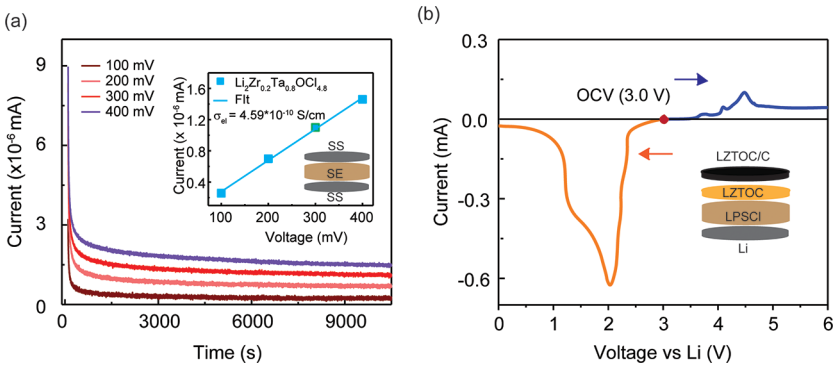

Figure 5. (a) DC polarization on a symmetric SS| $Li_2Zr_{0.2}Ta_{0.8}OCl_{4.8}$ |SS cell for determining the electronic conductivity, σ_{el}. The inset shows the $I-V$ curve of $Li_2Zr_{0.2}Ta_{0.8}OCl_{4.8}$ under different DC voltages with a linear fit. (b) Linear Sweep Voltammetry curve for evaluating the electrochemical stability window of $Li_2Zr_{0.2}Ta_{0.8}OCl_{4.8}$.

Lithium-Ion Transport Properties

Ion transport properties of LZTOC, LZOC, and LZC are determined using AC electrochemical impedance spectroscopy (EIS). Nyquist plots for LZTOC at temperatures ranging from −20 °C to 60 °C are shown in Figure 4a. At lower temperatures, the higher impedance values suggest slower lithium-ion diffusion. As the temperature increases, the impedance decreases, indicating increased ionic conductivity due to enhanced lithium-ion mobility. The observed trend aligns with Arrhenius-type ionic conduction, where conductivity increases with temperature.[36]

The Arrhenius plot in Figure 4b compares the temperature-dependent conductivity of LZTOC, LZOC, and LZC. LZTOC demonstrates the highest conductivity across the measured temperature range, confirming its superior lithium-ion transport properties. The linear trend in the plot suggests Arrhenius-type conduction, in which ionic transport is governed by thermally activated hopping. The slope of each line corresponds to the activation energy (E_a), with LZTOC exhibiting a lower activation barrier than LZOC and LZC. This implies that Ta^{5+} substitution in LZTOC not only enhances lithium mobility but also modifies the energy landscape for Li^+ migration.

The Nyquist plot for LZTOC at 25 °C, fitted using an equivalent circuit model, is shown in Figure 4c. No semicircle was observed in the high-frequency region, while the linear tail at low frequencies corresponds to electrode−electrolyte interfacial polarization. The equivalent circuit incorporates a resistor (R_1) to account for the intrinsic material resistance, whereas electrode−electrolyte polarization is represented by a constant-phase element (CPE_3), reflecting the system's nonideal capacitive response.[37] The lack of a semicircular feature in the high-frequency region is indicative of superionic conduction.[34] As the temperature decreases, a partial semicircle begins to appear in the high-frequency region (Figure S4a). An additional parallel resistor (R_2) and a constant phase element (CPE_2) were introduced between the existing resistor (R_1) and the terminal CPE_3. The capacitance associated with this element, on the order of 10^{-6} F/cm^2, suggests that it originates from the interface between the stainless-steel current collectors and the sample.[34] This capacitance does not reflect the intrinsic transport properties within the solid electrolyte. The close agreement between the experimental and fitted data validates the equivalent circuit model and confirms that LZTOC has low bulk resistance and favorable ionic transport characteristics. The plot in Figure 4d compares the RT (25 °C) ionic conductivity (mS/cm) and activation energy (E_a) for LZC, LZTOC, and LZOC. LZTOC shows the highest ionic conductivity (6.17 mS/cm) and the lowest activation energy (~0.30 eV), highlighting its efficient lithium-ion transport. The reduction in activation energy suggests that the potential landscape for the carrier ions in LZTOC is flatter. In contrast, LZOC and LZC exhibit lower conductivity, 0.4 and 0.1 mS/cm, respectively, and higher E_a, suggesting a less favorable lithium transport pathway or a more energy-intensive transport mechanism (Figure S4b).

The high ionic conductivity of LZTOC relative to LZC and LZOC can be attributed to several factors. First, relative to crystalline LZC, we found that oxygen substitution effectively promotes amorphization by altering the local structure, thereby increasing ionic conductivity in both oxyhalides, LZOC and LZTOC.[8] The high electronegativity of O^{2-} is typically associated with stronger electrostatic interactions with mobile cations, such as Li^+, which can increase migration barriers and, consequently, reduce ionic mobility in solid electrolytes. This is why, in many oxide-based systems, the incorporation of oxygen tends to hinder ion transport. However, in amorphous oxychloride systems, an intriguing phenomenon is observed. The addition of O^{2-} ions can enhance ionic conductivity, despite the inherent tendency of O^{2-} to impede ion movement.[34] As discussed in the Raman spectroscopy analysis, bridging oxygen atoms are integrated into extended polyhedral networks and do not directly interact with Li^+ ions. Second, prior studies suggest that $TaCl_5$ has a strong tendency to induce glass formation in salts, which likely contributes to the amorphous nature of LZTOC.[38] A key advantage of amorphous electrolytes over crystalline materials like LZC is their ability to minimize grain boundary impedance, leading to higher pellet densification and improved ionic conductivity.[39] We found that a subsequent heating operation at 300 °C to crystallize LZTOC significantly reduces ionic conductivity (Figure S5). Mechanochemical milling results in more disordered structures, which may also contribute to faster Li-ion motion.[9,24] Third, inductive effects arising from the electronegativity difference between Zr and Ta cations, which weaken Li-anion interactions,[19] may contribute to the enhanced ionic conductivity of LZTOC relative to LZOC. Cations with a higher ionic potential than Li tend to draw electrons away from the bridging X^{-n} ions (X = Cl^-, O^{2-}), weakening the Li−X bonds and thereby enhancing Li-ion transport.[24] The findings discussed above offer valuable

https://doi.org/10.1021/acs.chemmater.6c00149
Chem. Mater. 2026, 38, 7095−7103

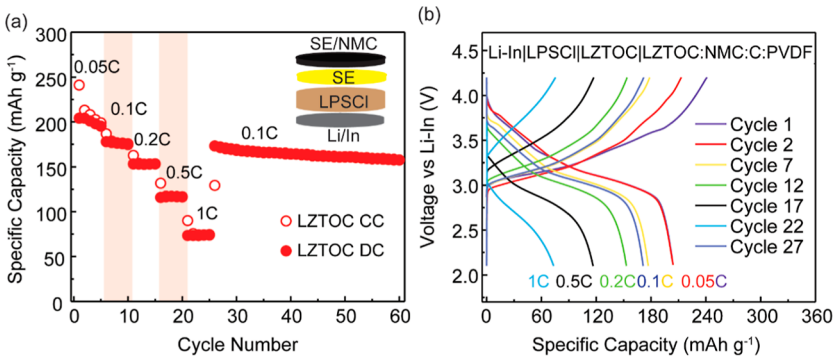

Figure 6. All-solid-state battery cycling performance of $Li_2Zr_{0.2}Ta_{0.8}OCl_{4.8}$ in a half cell made of NMC: LZTOC (1:1 wt %)|LZTOC|LPSC|Li−In alloy. (a) Rate capability plots and (b) selected voltage−capacity profiles at *C*-rates of 0.05, 0.1, 0.2, 0.5, and 1C.

mechanistic insights into the enhanced ionic conductivity observed in the amorphous oxyhalide family of materials.

Electrochemical Stability and Cycling Performance

Figure 5a shows the time-dependent current decay at different applied voltages (100−400 mV), indicating an initial capacitive response followed by stabilization, characteristic of an insulating material with minimal electronic conduction. The initial rapid relaxation of the current arose from ion polarization associated with the material's high ionic conductivity.[40] The inset plot shows a linear relationship between steady-state current and voltage, confirming ohmic behavior. From this, the electronic conductivity (σ_{el}) is calculated to be 4.59×10^{-10} S/cm, indicating that LZTOC has extremely low electronic conductivity, a desirable property for a solid electrolyte to prevent electronic leakage.[41] The symmetric SS/SE/SS (stainless steel/solid electrolyte/stainless steel) setup ensures that the measured current is purely electronic, ruling out ionic contributions. Both LZC and LZOC exhibit low electronic conductivity. Compared to the LZC halides, the oxyhalides demonstrate even lower electronic conductivity, making them more suitable candidates for solid electrolyte applications (Figure S6).

The linear sweep voltammetry curve (Figure 5b) assesses the electrochemical stability window of LZTOC by scanning the voltage against a Li reference electrode. The open-circuit voltage (OCV) of 3.0 V represents the equilibrium potential before any polarization occurs. The cathodic response (negative current) below 2.0 V suggests lithium insertion or possible reduction reactions, while the anodic response (positive current) beyond 3.8 V indicates oxidation or electrolyte decomposition.[10,22] This demonstrates that LZTOC remains electrochemically stable between ∼2.0 V and ∼3.8 V, making it a promising solid electrolyte candidate for high-voltage applications.

To assess its performance in ASSBs, LZTOC was integrated into a half-cell with an uncoated NMC cathode, functioning as both a catholyte and a separator. A thin layer of argyrodite Li_6PS_5Cl was introduced between LZTOC and the Li−In anode. In this setup, the composite cathode consists of 50 wt % NMC and 50 wt % SE; an equal mass ratio of NMC and LZTOC was used in the composite cathode to enhance ionic percolation and optimize lithium-ion transport.[42] The cell was cycled at cutoff potentials of 2.5−4.2 V vs Li−In at room temperature under ∼30 MPa stack pressure. The galvanostatic rate performance was determined at 0.05, 0.1, 0.2, 0.5, and 1C for five cycles each, with C = 275 mAh g^{-1} for NMC, followed by 0.05 C for long-term cycling.[24,43] Figure 6a,b shows the rate performance and the corresponding voltage profiles, respectively.

At 0.05 C, the cell delivers an initial charge capacity of 241 mAh/g and a discharge capacity of 204 mAh/g. As the *C*-rate increases from 0.05C to 1C, discharge capacity gradually declines, reaching 73.16 mAh/g at 1C, which is expected due to kinetic limitations in lithium transport. After returning to 0.1C, the discharge capacity recovers to ∼171 mAh/g at the 27th cycle and retains ∼88.9% of the initial capacity after 60 cycles. The cell also maintains a high Coulombic efficiency of ∼99.8%, highlighting LZTOC as a strong candidate for high-voltage-compatible solid electrolytes that support durable solid-state battery operation. The observed stability at high cutoff voltages can be attributed to the formation of a kinetically stabilized cathode-electrolyte interphase, consistent with prior literature on halide-based ASSBs.[44,45] Figure 6b shows the selected voltage profiles, confirming stable electrochemical behavior of the Li−In|Li_6PS_5Cl|SE|SE/NMC cell.

CONCLUSION

The systematic investigation of $Li_2Zr_{0.2}Ta_{0.8}OCl_{4.8}$ (LZTOC) establishes it as a high-performance amorphous oxychloride solid electrolyte accessible via a rapid, single-step 2 h mechanochemical synthesis. XRD highlights a clear structural evolution from crystalline Li_2ZrCl_6 to largely amorphous Li_2ZrOCl_4 upon oxygen incorporation and further to LZTOC with Ta^{5+} substitution, consistent with a strengthened glass-forming tendency in the oxychloride framework. Raman and MAS NMR suggest an amorphous network of Ta/Zr-centered polyhedra connected through oxygen-bridged motifs, forming a disordered yet percolative anion framework that enables fast Li^+ migration. Consequently, LZTOC delivers a high room-temperature ionic conductivity of 6.17 mS cm^{-1} with a low activation energy of ∼0.30 eV, consistent with accelerated ion dynamics observed by ^{7}Li T_1 relaxation.

When deployed as both a separator and catholyte in cells with uncoated NMC811, LZTOC enables stable cycling with 99.8% Coulombic efficiency and 88.9% capacity retention, demonstrating durable interfacial performance under practical operating conditions. Collectively, these results position LZTOC as a promising electrolyte platform for ASSBs and highlight the tunability of amorphous oxychloride frameworks through targeted cation substitution as a scalable pathway to further performance gains.

https://doi.org/10.1021/acs.chemmater.6c00149
Chem. Mater. 2026, 38, 7095−7103

■ ASSOCIATED CONTENT

Data Availability Statement

The data supporting this article have been included as part of the Supporting Information.

Supporting Information

The Supporting Information is available free of charge at https://pubs.acs.org/doi/10.1021/acs.chemmater.6c00149.

Selected PXRD patterns and Rietveld refinements, SEM images and EDS elemental mapping, EIS data, and DC polarization measurements data; ^{6}Li MAS NMR spectra, peak assignments, line width analysis, and phase composition data; NMR calculations; and crystallographic parameters from Rietveld refinement of Li_2ZrCl_6 (PDF)

■ AUTHOR INFORMATION

Corresponding Author

Yan-Yan Hu − *Department of Chemistry and Biochemistry, Florida State University, Tallahassee, Florida 32306, United States; Materials Science and Engineering Program, Florida State University, Tallahassee, Florida 32310, United States; Center of Interdisciplinary Magnetic Resonance, National High Magnetic Field Laboratory, Tallahassee, Florida 32310, United States;* orcid.org/0000-0003-0677-5897; Email: hu@chem.fsu.edu

Authors

Thilina N.D.D. Gamaralalage − *Department of Chemistry and Biochemistry, Florida State University, Tallahassee, Florida 32306, United States*

Bright O. Ogbolu − *Department of Chemistry and Biochemistry, Florida State University, Tallahassee, Florida 32306, United States*

M.D. Mahinur Islam − *Department of Chemistry and Biochemistry, Florida State University, Tallahassee, Florida 32306, United States*

Tehreem Toheed − *Department of Chemistry and Biochemistry, Florida State University, Tallahassee, Florida 32306, United States*

Joey Peterson − *Department of Chemistry and Biochemistry, Florida State University, Tallahassee, Florida 32306, United States;* orcid.org/0009-0000-7473-6967

Tej P. Poudel − *Materials Science and Engineering Program, Florida State University, Tallahassee, Florida 32310, United States*

Complete contact information is available at: https://pubs.acs.org/10.1021/acs.chemmater.6c00149

Author Contributions

‖T.N.D.D.G. and B.O.O. contributed equally to this work.

Notes

The authors declare no competing financial interest.

■ ACKNOWLEDGMENTS

Support from the National Science Foundation (DMR-2319151) is gratefully acknowledged. Solid-state NMR data were collected at the National High Magnetic Field Laboratory, which is funded by NSF Cooperative Agreements DMR-1644779 and DMR-2128556 and by the State of Florida. This research includes Raman experiments carried out in the Materials Characterization Laboratory at the Florida State University Department of Chemistry and Biochemistry (FSU075000MAC), with technical assistance provided by Raaj Winfred.

■ REFERENCES

(1) Tanaka, Y.; Ueno, K.; Mizuno, K.; Takeuchi, K.; Asano, T.; Sakai, A. New Oxyhalide Solid Electrolytes with High Lithium Ionic Conductivity > 10 mS cm^{-1} for All-Solid-State Batteries. *Angew. Chem., Int. Ed.* **2023**, *62*, No. e202217581.

(2) Li, L.; Jiang, Z.; Yang, J.; Liu, C.; Luo, Q.; Li, S.; Zhang, L.; Chen, X.; Cheng, S.; Yu, C. A Rapid Synthesis of Amorphous $LiTaOCl_4$ Solid Electrolytes Through a Two-Step Reaction Pathway for High-Rate and Long-Cycling Lithium Batteries. *Adv. Funct. Mater.* **2025**, *35*, 2410008.

(3) Wu, E. A.; Banerjee, S.; Tang, H.; Richardson, P. M.; Doux, J. M.; Qi, J.; Zhu, Z.; Grenier, A.; Li, Y.; Zhao, E.; et al. A Stable Cathode-Solid Electrolyte Composite for High-Voltage, Long-Cycle-Life Solid-State Sodium-Ion Batteries. *Nat. Commun.* **2021**, *12*, 1256.

(4) Riegger, L. M.; Schlem, R.; Sann, J.; Zeier, W. G.; Janek, J. Lithium-Metal Anode Instability of the Superionic Halide Solid Electrolytes and the Implications for Solid-State Batteries. *Angew. Chem., Int. Ed.* **2021**, *60*, 6718−6723.

(5) Luo, X.; Zhong, Y.; Wang, X.; Xia, X.; Gu, C.; Tu, J. Ionic Conductivity Enhancement of Li2ZrCl6 Halide Electrolytes via Mechanochemical Synthesis for All-Solid-State Lithium−Metal Batteries. *ACS Appl. Mater. Interfaces* **2022**, *14*, 49839−49846.

(6) Li, X.; Liang, J.; Luo, J.; Norouzi Banis, M.; Wang, C.; Li, W.; Deng, S.; Yu, C.; Zhao, F.; Hu, Y.; et al. Air-Stable Li_3InCl_6 Electrolyte with High Voltage Compatibility for All-Solid-State Batteries. *Energy Environ. Sci.* **2019**, *12*, 2665−2671.

(7) Hu, L.; Zhu, J.; Duan, C.; Zhu, J.; Wang, J.; Wang, K.; Gu, Z.; Xi, Z.; Hao, J.; Chen, Y.; et al. Revealing the Pnma Crystal Structure and Ion-Transport Mechanism of the Li_3YCl_6 Solid Electrolyte. *Cell Rep. Phys. Sci.* **2023**, *4*, 101428.

(8) Hu, L.; Wang, J.; Wang, K.; Gu, Z.; Xi, Z.; Li, H.; Chen, F.; Wang, Y.; Li, Z.; Ma, C. A Cost-Effective, Ionically Conductive and Compressible Oxychloride Solid-State Electrolyte for Stable All-Solid-State Lithium-Based Batteries. *Nat. Commun.* **2023**, *14*, 3807.

(9) Kwak, H.; Kim, J. S.; Han, D.; Kim, J. S.; Park, J.; Kwon, G.; Bak, S. M.; Heo, U.; Park, C.; Lee, H. W.; et al. Boosting the Interfacial Superionic Conduction of Halide Solid Electrolytes for All-Solid-State Batteries. *Nat. Commun.* **2023**, *14*, 2459.

(10) Kwak, H.; Han, D.; Lyoo, J.; Park, J.; Jung, S. H.; Han, Y.; Kwon, G.; Kim, H.; Hong, S. T.; Nam, K. W.; et al. New Cost-Effective Halide Solid Electrolytes for All-Solid-State Batteries: Mechanochemically Prepared Fe^{3+}-Substituted Li_2ZrCl_6. *Adv. Energy Mater.* **2021**, *11*, 2003190.

(11) Yu, Y.; Huang, Y.; Xu, Z.; Wu, Z.; Wang, Z.; Shao, G. A High-Voltage Solid State Electrolyte Based on Spinel-Like Chloride Made of Low-Cost and Abundant Resources. *Adv. Funct. Mater.* **2024**, *34*, 2315512.

(12) Yao, Z.; Jia, Q.; Xiang, J.; Tu, F.; Shi, J.; Zhang, Y.; Huang, J.; Jiang, Y.; Gong, W.; Yang, D. High Ionic Conductivity in Li_2ZrCl_6 via La^{3+} Doping for All-Solid-State Lithium Metal Batteries. *J. Electron. Mater.* **2025**, *54*, 1021−1028.

(13) Liu, X.; Mi, F.; Sun, C. A Cost-Effective Ca-Doped Li_2ZrCl_6 Halide Solid Electrolyte for All-Solid-State Lithium Batteries. *Chem. Commu.* **2025**, *61*, 1144−1147.

(14) Yang, X.; Chen, Y.; Wei, G.; Diallo, M. S.; Avdeev, M.; Hau, H. M.; Qiu, H.; Ji, H.; Ceder, G. Harnessing Cation Disorder for Enhancing Ionic Conductivity in Lithium Inverse Spinel Halides. *ACS Energy Lett.* **2025**, *10*, 1338−1346.

(15) Huang, L.; Barker, K.; Liu, X.; Jian, Y.; Skinner, S. J.; Ryan, M. P.; Huang, C. A. Mixed-Anion Strategy for Constructing Rapid Ion-Conducting Na Solid-State Electrolyte. *Chem. Inorg. Mater.* **2025**, *6*, 100102.

(16) Wang, J.; Chen, F.; Hu, L.; Ma, C. Alternate Crystal Structure Achieving Ionic Conductivity above 1 mS cm^{-1} in Cost-Effective Zr-Based Chloride Solid Electrolytes. *Nano Lett.* **2023**, *23*, 6081−6087.
(17) Hussain, F.; Zhu, J.; Zhao, Y.; Xia, W. Exploring Superionic Conduction in Lithium Oxyhalide Solid Electrolytes Considering Composition and Structural Factors. *njp Comput. Mater.* **2024**, *10*, 148.
(18) Wu, Y.; Wang, L.; Wei, S.; Bi, X.; Zhuo, H.; Xiao, W.; Yu, T.; Duan, Y.; Zhao, C.; Yang, R.; et al. Exploiting the Mixed Entropy Strategy for the Design of Fast Ion Conductors. *Adv. Energy Mater.* **2024**, *14*, 2401528.
(19) Wang, Q.; Zhou, Y.; Wang, X.; Guo, H.; Gong, S.; Yao, Z.; Wu, F.; Wang, J.; Ganapathy, S.; Bai, X.; et al. Designing Lithium Halide Solid Electrolytes. *Nat. Commun.* **2024**, *15*, 1050.
(20) Zhao, F.; Zhang, S.; Wang, S.; Andrei, C. M.; Yuan, H.; Zhou, J.; Wang, J.; Zhuo, Z.; Zhong, Y.; Su, H.; et al. Revealing Unprecedented Cathode Interface Behavior in All-Solid-State Batteries with Oxychloride Solid Electrolytes. *Energy Environ. Sci.* **2024**, *17*, 4055−4063.
(21) Xue, W.; Cui, Y.; Long, Z.; Shan, H.; Chamidah, N.; Yamamoto, K.; Kotobuki, M.; Li, H.; Hu, N.; Song, S. New Oxyhalide Solid Electrolytes with Enhanced Conductivity for All-Solid-State Batteries. *J. Phys. Chem. Lett.* **2025**, *16*, 8283−8289.
(22) Deng, S.; Jiang, M.; Chen, N.; Li, W.; Zheng, M.; Chen, W.; Li, R.; Huang, H.; Wang, J.; Singh, C. V.; et al. Regulating Electronic Conductivity at Cathode Interface for Low-Temperature Halide-Based All-Solid-State Batteries. *Adv. Funct. Mater.* **2022**, *32*, 2205594.
(23) Dietrich, C.; Weber, D. A.; Sedlmaier, S. J.; Indris, S.; Culver, S. P.; Walter, D.; Janek, J.; Zeier, W. G. Lithium Ion Conductivity in Li2S-P2S5 Glasses-Building Units and Local Structure Evolution during the Crystallization of Superionic Conductors Li3PS4, Li7P3S11 and Li4P2S7. *J. Mater. Chem. Mater.* **2017**, *5*, 18111−18119.
(24) Ridley, P.; Duong, G.; Ko, S. L.; Sam Oh, J. A.; Deysher, G.; Griffith, K. J.; Meng, Y. S. Tailoring Chloride Solid Electrolytes for Reversible Redox. *J. Am. Chem. Soc.* **2025**, *147*, 19508−19519.
(25) Wang, K.; Ren, Q.; Gu, Z.; Duan, C.; Wang, J.; Zhu, F.; Fu, Y.; Hao, J.; Zhu, J.; He, L.; et al. A Cost-Effective and Humidity-Tolerant Chloride Solid Electrolyte for Lithium Batteries. *Nat. Commun.* **2021**, *12*, 4410.
(26) Lin, X.; Zhao, Y.; Wang, C.; Luo, J.; Fu, J.; Xiao, B.; Gao, Y.; Li, W.; Zhang, S.; Xu, J.; et al. A Dual Anion Chemistry-Based Superionic Glass Enabling Long-Cycling All-Solid-State Sodium-Ion Batteries. *Angew. Chem., Int. Ed.* **2024**, *63*, No. e202314181.
(27) Patel, S. V.; Banerjee, S.; Liu, H.; Wang, P.; Chien, P. H.; Feng, X.; Liu, J.; Ong, S. P.; Hu, Y. Y. Tunable Lithium-Ion Transport in Mixed-Halide Argyrodites $Li_{6-X}PS_{5-X}ClBr_x$: An Unusual Compositional Space. *Chem. Mater.* **2021**, *33*, 1435−1443.
(28) Babushkina, O. B.; Ekres, S.; Nauer, G. E. Raman spectroscopy of the mixtures (x)1-butyl-1-methylpyrrolidinium chloride-(1 - X)$TaCl_5$ in solid and molten states. *J. Phys. Chem. A* **2008**, *112*, 8288−8294.
(29) Ogbolu, B. O.; Gamaralalage, T. N. D. D.; Islam, M. M.; Toheed, T.; Sariego, J.; Poudel, T. P.; Francisco, B. E.; Hu, Y. Y. $Li_2TaS_{1-X}O_xCl_5$: Triple-Anion Glassy Superionic Conductors for High-Performance Solid-State Batteries. *ACS Mater. Lett.* **2025**, *7*, 4029−4036.
(30) Wetherall, K. M.; Doughty, P.; Mountjoy, G.; Bettinelli, M.; Speghini, A.; Casula, M. F.; Cesare-Marincola, F.; Locci, E.; Newport, R. J. The Atomic Structure of Niobium and Tantalum Containing Borophosphate Glasses. *J. Phys.: Condens. Matter* **2009**, *21*, 375106.
(31) Zhang, X.; Chen, Q.; Zhang, S. Ta_2O_5 Nanocrystals Strengthened Mechanical, Magnetic, and Radiation Shielding Properties of Heavy Metal Oxide Glass. *Molecules* **2021**, *26*, 4494.
(32) Tan, Y.; Gatts, J.; Fu, C.; Deng, Z.; Li, S.; Lou, C.; Tang, M.; Xiang, H.; Cho, K.; Toher, C.; et al. Dual-Anion Sodium Halide-Based Solid Electrolytes With High Ionic Conductivity and High-Voltage Stability. *Small* **2025**, *21*, 2504677.
(33) Balachandran, U.; Eror, N. G. A Study of the Crystal Structure of B-Ta_2O_5 by Vibrational Spectroscopy and X-ray Diffraction. *J. Mater. Sci. Lett.* **1982**, *1*, 219−222.
(34) Huang, Z.; Yadav, N.; Song, P.; Akamatsu, H.; Hayashi, K.; Gorai, P.; Ohno, S. Oxygen-Mediated Structural Modulation and Ionic Transport in XNa_2O-$TaCl_5$ Glass Electrolytes. *J. Am. Chem. Soc.* **2025**, *147*, 43391−43399.
(35) Bloembergen, N.; Purcell, E. M.; Pound, R. V. Relaxation Effects in Nuclear Magnetic Resonance Absorption. *Phys. Rev.* **1948**, *73*, 679−712.
(36) Ogbolu, B. O.; Poudel, T. P.; Dikella, T. N. D. D.; Truong, E.; Chen, Y.; Hou, D.; Li, T.; Liu, Y.; Gabriel, E.; Xiong, H.; et al. Tailoring Ion Transport in $Li_{3-3y}Ho_{1+y}Cl_{6-X}Br_x$ via Transition-Metal Free Structural Planes and Charge Carrier Distribution. *Adv. Sci.* **2024**, *12*, 2409668.
(37) Schlem, R.; Banik, A.; Ohno, S.; Suard, E.; Zeier, W. G. Insights into the Lithium Sub-Structure of Superionic Conductors Li_3YCl_6 and Li_3YBr_6. *Chem. Mater.* **2021**, *33*, 327−337.
(38) Zhao, T.; Samanta, B.; de Irujo-Labalde, X. M.; Whang, G.; Yadav, N.; Kraft, M. A.; Adelhelm, P.; Hansen, M. R.; Zeier, W. G. Sodium Metal Oxyhalides $NaMOCl_4$ (M = Nb, Ta) with High Ionic Conductivities. *ACS Mater. Lett.* **2024**, *6*, 3683−3689.
(39) Yu, T.; Liu, Y.; Li, H.; Sun, Y.; Guo, S.; Zhou, H. Ductile Inorganic Solid Electrolytes for All-Solid-State Lithium Batteries. *Chem. Rev.* **2025**, *125*, 3595−3662.
(40) Makino, K.; Tanibata, N.; Natori, T.; Nakano, T.; Takeda, H.; Nakayama, M. Multicomponentization of a Super-Na Ionic Conductor Chloride $NaTaCl_6$, Enhancing Ionic Conductivity and Electronic Resistivity. *J. Mater. Chem. A* **2025**, *13*, 22924−22930.
(41) Culver, S. P.; Koerver, R.; Krauskopf, T.; Zeier, W. G. Designing Ionic Conductors: The Interplay between Structural Phenomena and Interfaces in Thiophosphate-Based Solid-State Batteries. *Chem. Mater.* **2018**, *30*, 4179−4192.
(42) Minnmann, P.; Quillman, L.; Burkhardt, S.; Richter, F. H.; Janek, J. Editors' Choice−Quantifying the Impact of Charge Transport Bottlenecks in Composite Cathodes of All-Solid-State Batteries. *J. Electrochem. Soc.* **2021**, *168*, 040537.
(43) Winkowska-Struzik, M.; Buchberger, D. A.; Uhrynowski, W.; Struzik, M.; Czerwinski, A. Air Storage Impact on Surface Evolution of Stoichiometric and Li-Rich NMC811. *ACS Omega* **2024**, *9*, 50334−50348.
(44) Zhou, L.; Zuo, T.; Li, C.; Zhang, Q.; Janek, J.; Nazar, L. F. $Li_{3-x}Zr_x(Ho/Lu)_{1-x}Cl_6$ Solid Electrolytes Enable Ultrahigh-Loading Solid-State Batteries with a Prelithiated Si Anode. *ACS Energy Lett.* **2023**, *8*, 3102−3111.
(45) Zhao, F.; Zhang, S.; Wang, S.; Reid, J. W.; Xia, W.; Liu, J.; King, G.; Kaduk, J. A.; Liang, J.; Luo, J.; et al. Anion Sublattice Design Enables Superionic Conductivity in Crystalline Oxyhalides. *Science* **2025**, *390*, 199−204.